Extending a Mole-Based Design Framework to Enable the Design of Versatile Antagonistic SMA Actuator Architectures

Joachim Schmidt
Development - Products and Production
Dcubed GmbH
Germering, Germany
joachim.schmidt@dcubed-space.com

***Abstract*—Adaptive space structures with reversible shape morphing are essential to optimize spacecraft performance across varying mission phases [1]. However, compact and lightweight actuation remains a significant challenge. Shape memory alloy (SMA) actuators have emerged as promising solutions due to their high power-to-weight ratios and smooth actuation [2]. In this work, we extend the model-based design framework proposed by Schmidt [3] to evaluate and compare different actuator architectures. The objective is to estimate the performance of each architecture in terms of efficiency, power mass density, and power volume density. The spring-based architecture originally proposed is compared against torsional and tensional alternatives. Results show that while the torsional architecture does not significantly improve efficiency or power mass density, it does offer higher power volume density. The tensional architecture provides a 100% increase in all three metrics when compared to the torsional design. This comparative analysis supports the selection of appropriate antagonistic SMA actuator configurations based on mission-specific design priorities.**

***Index Terms*—Shape Memory Alloy, Antagonistic Actuation, Bistable Structures, Adaptive Mechanisms, Morphing Aerospace Structures**

I. Introduction

Modern spacecraft require systems that can adapt to varying mission demands. Adaptive structures capable of reversible shape morphing offer significant performance enhancements for instruments such as antennas, solar arrays, and radiators. However, a major barrier to their implementation is the lack of reliable, compact, and efficient actuators. Traditional actuators like motors and gear trains are precise but bulky and consume considerable power.

Shape Memory Alloys (SMAs) are an attractive alternative due to their high specific force, compact form factor, and low noise during actuation. They have been extensively used in space-qualified hold-down and release mechanisms (HDRMs) [4], [5]. However, applications in reversible morphing structures remain limited, particularly due to the complexity of controlling SMA actuation and the lack of predictive models for actuator behavior.

The paper presented by [3] introduces a model-based design framework for antagonistic SMA actuators that operate bistable structures. The antagonistic configuration enables two stable equilibrium positions with no input power, making it ideal for low-energy applications. The framework utilizes a phenomenological constitutive model to accurately predict the force-displacement behavior of SMA springs and determines actuator output through force equilibrium analysis.

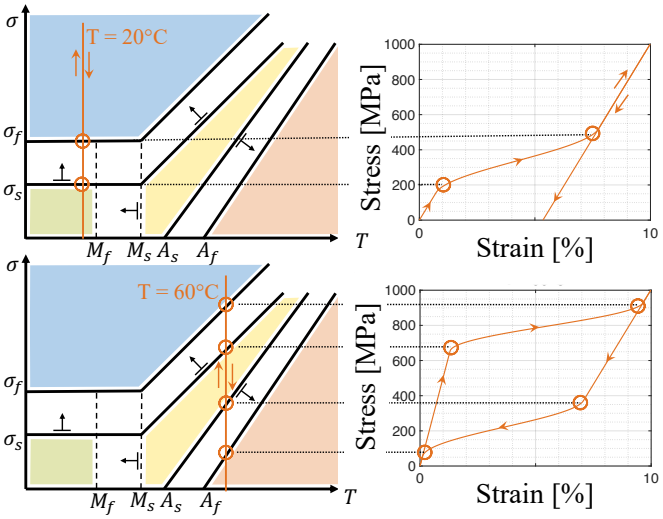

Fig. 1. Phase diagram for NiTi shape memory alloys along corresponding phenomenological stress strain behavior. Adopted by [7]

II. Modeling Framework

III. Thermomechanical Modeling of Antagonistic SMA Actuation

Shape Memory Alloys (SMAs) exhibit phase transitions between austenite and martensite, enabling two unique behaviors: the shape memory effect (strain recovery upon heating) and pseudoelasticity (large, reversible deformation at high temperatures) [6]. These effects depend on four characteristic temperatures: M_s, M_f, A_s, and A_f. Figure 1 shows, how the distinct material properties are linked to:

A. Constitutive Model Under Isothermal Conditions

We adopt Brinson's model [7], which separates martensite into twinned (ξ_T) and detwinned (ξ_S) components, with total

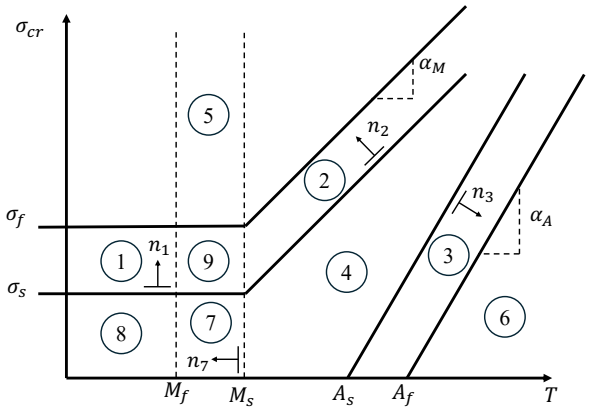

Fig. 2. Phase diagram for NiTi shape memory alloys.

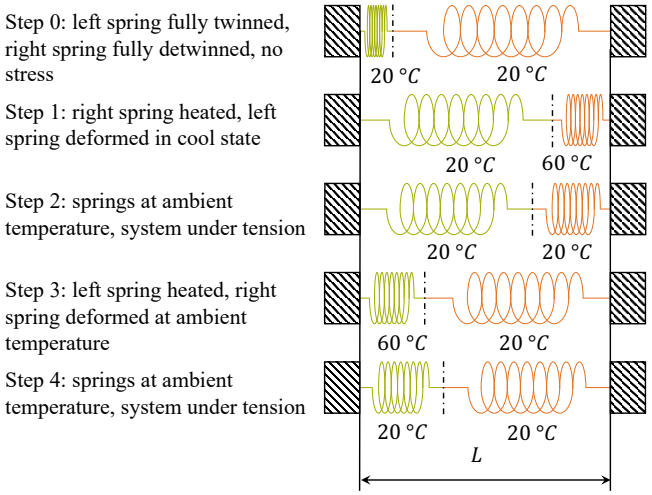

Fig. 3. Operating principle of an antagonistic SMA actuator.

volume fraction $\xi = \xi_T + \xi_S$. Cosine functions describe phase transitions between regions in the phase diagram (Fig. 2). Transitions occur when the thermo-mechanical load path aligns with phase transformation vectors also depicted in Figure 2.

Under isothermal assumptions, detwinned martensite forms via stress-driven equations in Regions 1 and 3, while twinned martensite and austenite form in Regions 2 and 4 [8]:

$$\xi_S = \frac{1-\xi_{S0}}{2}\cos\left(\frac{\pi}{\sigma_s-\sigma_f}(\sigma-\sigma_f)\right)+\frac{1+\xi_{S0}}{2} \quad (1)$$

$$\xi_T = \frac{1-\xi_{T0}-\xi_{S0}}{2}\left[\cos\left(\frac{\pi}{M_s-M_f}(T-M_f)\right)+1\right]+\xi_{T0} \quad (2)$$

$$\xi = \frac{\xi_0}{2}\left[\cos\left(\frac{\pi}{A_f-A_s}(T-A_s-\sigma/c_A)\right)+1\right] \quad (3)$$

Stress is related to strain through the phase-dependent modulus $E(\xi)$ [7]:

$$\sigma-\sigma_0 = E(\xi)\varepsilon - E(\xi_0)\varepsilon_0 - \varepsilon_L E(\xi)\xi_S + \varepsilon_L E(\xi_0)\xi_{S0} \quad (4)$$

$$E(\xi) = E_A + \xi(E_M - E_A) \quad (5)$$

B. Spring Model and Antagonistic Actuation

For SMA springs, the constitutive model adapts to spring deflection δ:

$$F-F_0 = D(\xi)\delta - D(\xi_0)\delta_0 - \delta_L D(\xi)\xi_S + \delta_L D(\xi_0)\xi_{S0} \quad (6)$$

An extended force-pitch relation accounts for geometric nonlinearity [9]:

$$F = \frac{\pi d^4}{8D_i^2}G\frac{\cos^2\alpha_i(\sin\alpha_f-\sin\alpha_i)}{\cos^2\alpha_f\left(\cos^2\alpha_f+\sin^2\alpha_f/(1+\nu)\right)} \quad (7)$$

Two springs in series define the antagonistic actuator. Equilibrium requires equal forces and fixed total length. During actuation (Steps 0–4), each spring alternates between pseudoelastic and shape-memory behavior. The actuator stroke is defined as the displacement difference between stable equilibrium points.

C. Cyclic Training and Numerical Implementation

Repeated cycling reduces actuator stroke linearly by 0.5% per cycle [10], [11]. The Matlab implementation simulates force steps, updating ξ values iteratively and computing displacements via the constitutive and spring models.

IV. Baseline Architecture: Spring Geometry

A. Shear Strain - Pitch Angle Relationship in SMA Coil Springs

To understand the deformation behavior of a Shape Memory Alloy (SMA) coil spring actuator, the relationship between *shear strain* γ and the *pitch angle* α_f is analyzed using a geometric model adapted from An et al. [9]. The model considers large deformations due to actuation and captures nonlinearities arising from the helical geometry.

The shear strain γ as a function of the pitch angle is given by:

$$\gamma = \frac{1}{C}\cdot\frac{\cos^2\alpha_i(\sin\alpha_f-\sin\alpha_i)}{\cos^2\alpha_f\left(\cos^2\alpha_f+\frac{\sin^2\alpha_f}{1+\nu}\right)} \quad (8)$$

Where:

- γ: Shear strain (–)
- $C = \frac{D}{d}$: Spring index (–), the ratio of spring diameter to wire diameter
- D: Coil diameter, 7 mm
- d: Wire diameter (gauge), 1 mm
- α_i: Initial pitch angle (rad)
- α_f: Current pitch angle (rad)
- ν: Poisson's ratio, assumed to be 0.5 for incompressible SMA material

The *initial pitch angle* α_i is calculated from the initial spring length L_0, the number of coils n, and the coil diameter D, using:

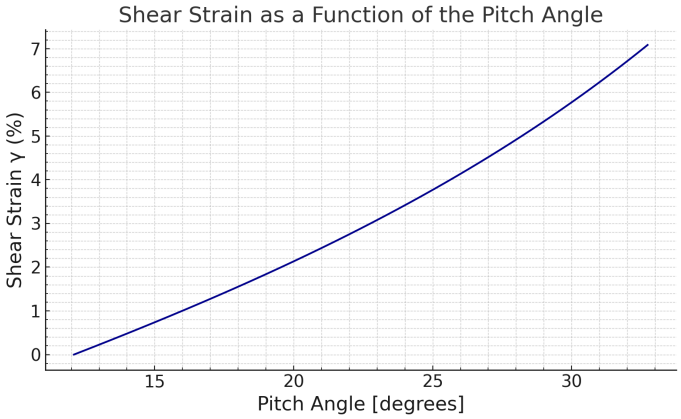

Fig. 4. Shear strain γ vs. pitch angle α_f for an SMA coil spring with specified parameters.

$$\alpha_i = \tan^{-1}\left(\frac{L_0/(2n)}{D}\right) \tag{9}$$

Given:

- $L_0 = 17$ mm (initial spring length)
- $n = 10$ (number of active coils)
- $D = 7$ mm

Substituting these values gives:

$$\alpha_i = \tan^{-1}\left(\frac{17/(2\cdot 10)}{7}\right) = \tan^{-1}(0.1214) \approx 6.93^\circ$$

Similarly, the *maximum pitch angle* $\alpha_{f,\max}$ is calculated using the extended spring length $L_{\max} = 90$ mm:

$$\alpha_{f,\max} = \tan^{-1}\left(\frac{90/20}{7}\right) = \tan^{-1}(0.6429) \approx 32.86^\circ$$

Using Equation 8, the shear strain γ was computed over a range of α_f values from $\alpha_i \approx 6.93^\circ$ to $\alpha_{f,\max} \approx 32.86^\circ$. The resulting relationship, shown in Figure 4, demonstrates the nonlinear increase in shear strain with pitch angle due to the geometry of the coil. The strain values were also expressed as percentages for clarity.

The plot shows that in the antagonistic benchtop setup used by Schmidt [3], shear strains of up to **7%** were observed. This value includes both the *residual strain* and the *elastic deformation* of the spring, as the system remains under constant tension.

B. Actuator Performance Metrics

The developed antagonistic shape memory alloy (SMA) actuator was characterized in terms of key performance metrics including stroke, force output, power consumption, volume, and mass. These metrics were used to evaluate its suitability for driving bistable morphing structures in space applications and to enable quantitative comparison to conventional actuation technologies.

At the start of its operational life, the actuator achieved a maximum stroke of $30\,\mathrm{mm}$ and delivered a peak output force of $22\,\mathrm{N}$. After 75 actuation cycles, the stroke stabilized at $17\,\mathrm{mm}$ due to SMA training effects. At room temperature, the actuator consumed $3\,\mathrm{W}$ over a typical $18\,\mathrm{s}$ actuation period. In cold conditions ($-20\,^\circ\mathrm{C}$), power consumption increased to $14\,\mathrm{W}$ due to higher thermal losses. Assuming linear force decay from $22\,\mathrm{N}$ to zero over the $30\,\mathrm{mm}$ stroke, the average mechanical power output was approximately $18.3\,\mathrm{mW}$.

The active parts of the actuator assembly has a total mass of $4.5\,\mathrm{g}$ and occupied a volume of $3.42\,\mathrm{cm}^3$, resulting in a power mass density of $4.07\,\mathrm{W\,kg}^{-1}$ and a power volume density of $0.87\,\mathrm{mW\,cm}^{-3}$.

These metrics demonstrate that the developed SMA actuator exhibits competitive performance compared to miniaturized commercial linear actuators while offering unique advantages for space applications, such as silent operation, compact packaging, and mechanical bistability.

V. Alternative Architectures

A. Torsional Architecture

To investigate the efficiency of the torsional architecture and compare it with the baseline spring configuration, the shear stress distribution within the SMA material is analyzed. Fundamentally, both architectures operate under torsional loading: in the spring-based design, torsion arises from helical deformation, while in the torsional architecture, it results from direct torque application to a cylindrical or tubular SMA member.

The critical question is whether the spring geometry can generate enough shear strain to fully exploit the recoverable deformation range of the SMA. As demonstrated in the baseline actuator designed by Schmidt [3], the spring geometry achieves a shear strain of up to 7%, which is close to the maximum recoverable strain for NiTi-based SMAs. This suggests that even though the torsional architecture offers direct control over applied torque, it does not unlock a fundamentally higher strain potential if the spring geometry has already reached the material limit.

Figure 5 illustrates the shear stress distribution across a circular SMA cross-section during three distinct phases of torsional loading. In illustration (a), the deformation is purely elastic: shear stress increases linearly with radial position, and the stress-strain relationship remains linear. In illustration (b), the onset of detwinning is observed, and the shear stress distribution becomes nonlinear, indicating the emergence of inelastic material behavior. In illustration (c), the material is fully detwinned and enters a new linear regime where additional elastic deformation occurs in the detwinned martensitic phase.

Although the actual stress distribution is nonlinear during detwinning, a linear approximation is employed to estimate performance metrics. This approach, often referred to as quasilinear pseudoelastic modeling, simplifies the evaluation of efficiency by treating the complex phase transformation behavior as linearly elastic. In this context, it's important to note that the maximum shear stress—and thus the maximum

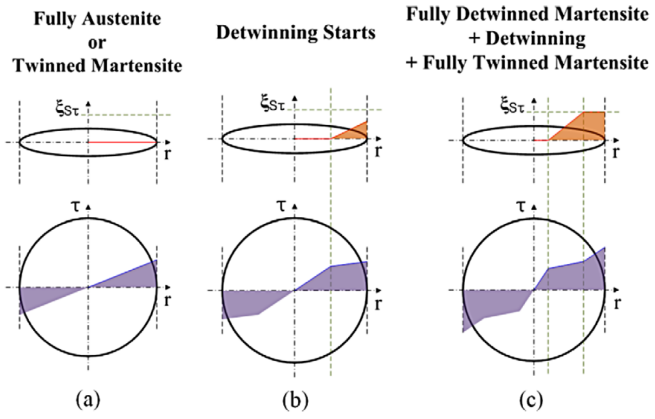

Fig. 5. Distributions of shear stress and martensitic volume fraction: (a) Elastic shear stress distribution in austenite at elevated temperature or in twinned martensite at low temperature (b) Nonlinear shear stress distribution during the detwinning process (c) Two distinct elastic shear stress profiles observed upon completion of detwinning. Adapted by [9]

recoverable shear strain—is only reached at the outer radius of the circular cross-section. The shear stress tapers off toward the neutral axis at the center, where it effectively drops to zero.

This distribution imposes a fundamental efficiency constraint: only a fraction of the material volume is utilized at its full potential. As a result, the theoretical mass efficiency of the torsional architecture is reduced by at least 50% compared to an idealized case where the entire cross-section experiences uniform, full-range shear deformation. This limitation is intrinsic to torsional loading and applies equally to spring geometries and direct torsional members.

In conclusion, the torsional architecture does not offer improved mass efficiency over a well-designed spring architecture, assuming the spring geometry is capable of producing the maximum usable shear strain. However, because the torsional actuator does not involve coiling and can be more compact in form, it offers improved volume efficiency. This makes it advantageous in applications where packaging constraints dominate over mass constraints.

B. Tensional Architecture

In the tensional architecture, the SMA member is subjected to a direct axial force rather than a torque. Unlike the spring and torsional architectures—which rely on shear stresses generated by torsion—this configuration loads the material in pure tension. As a result, the entire cross-section of the SMA experiences uniform axial stress, assuming a symmetrical, isotropic, and homogeneous material. This stress distribution leads to a uniform strain field across the cross-section.

One of the principal advantages of this architecture is that it enables the full utilization of the recoverable strain capacity of the SMA material, typically in the range of 6–7%. In contrast to the torsional architecture—where only the outermost fibers experience maximum shear strain—tensile loading ensures that the entire volume of the active material contributes to actuation. This makes the architecture inherently

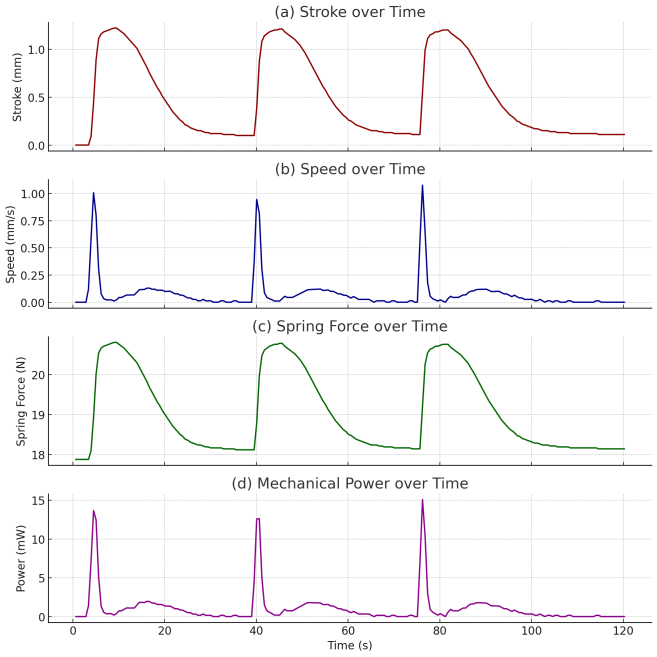

Fig. 6. Performance of the SMA wire during three thermal cycles in the tensional test setup.

more mass-efficient. In fact, theoretical considerations indicate that it offers at least a twofold improvement in efficiency over architectures with shear-limited stress distributions.

To experimentally investigate the performance of the tensional architecture, a test setup was developed in which an SMA wire was mounted antagonistically with a linear elastic spring. The wire was subjected to thermal cycling by resistive heating and ambient cooling, and its displacement was measured throughout the cycle. Due to the mechanical constraint imposed by the spring, the displacement of the SMA wire can be directly translated into the force acting on it via Hooke's Law.

By taking the time derivative of the measured displacement and multiplying it by the corresponding force, the instantaneous mechanical power output of the SMA was computed. This data was then used to calculate three key performance metrics: power density, power mass density, and power volume density. These values were directly compared to those obtained for the spring-based actuator.

Figure 6 shows the performance of the SMA wire undergoing thermal cycling across three actuation cycles. Plot A displays the stroke over time, showing a rapid increase during the heating phase and a gradual decrease during cooling. Each cycle includes an active heating phase of approximately 5 seconds followed by a 40-second cool-down period. Plot B shows the velocity over time, where a spike is observed during each heating phase, corresponding to rapid contraction. Plot C illustrates the spring force over time, which correlates linearly with displacement due to the spring's linear stiffness. Plot D shows the resulting mechanical power, calculated as the product of spring force and velocity. Each heating phase is

TABLE I
COMPARISON OF ACTUATOR ARCHITECTURES

Type	Mass	Stroke	Power	W/kg	mW/cm^3
Spring SMA [3]	4.5 g	30 mm	18.3 mW	4.07	0.87
Tensional SMA	0.04 g	1.5 mm	4.7 mW	**124.52**	**277.19**
LA 30 Motor [13]	24 g	30 mm	400 mW	16.66	35.1

marked by a distinct power spike reaching up to $15\,\mathrm{mW}$. The average mechanical power output during the 5-second heating periods is approximately $4.7\,\mathrm{mW}$. Since the SMA wire used in this test weighs only $0.0377\,\mathrm{g}$, this corresponds to a mass efficiency of $124.52\,\mathrm{W\,kg^{-1}}$.

VI. CONCLUSION AND COMPARRISON

This work presented a model-based evaluation of three different SMA actuator architectures—spring-based, torsional, and tensional—with a focus on reversible actuation of bistable structures. Each architecture was assessed in terms of its actuation efficiency, power density, and mechanical output.

While the spring and torsional architectures both rely on shear deformation due to torsional loading, the tensional architecture uniquely applies uniform axial stress across the full cross-section of the SMA material. This allows it to utilize the full recoverable strain range of the alloy, resulting in significantly higher mass and power efficiency.

However, the analysis also revealed that performance metrics are not exclusively dependent on the actuator architecture. System-level parameters such as total actuator mass and the mass of active elements appear to play a critical role. For instance, although the spring architecture was designed to produce a similar force to the tensional setup, the active SMA mass decreased from $4.5\,\mathrm{g}$ to only $0.0377\,\mathrm{g}$ in the tensional system. This dramatic reduction in system mass was accompanied by a substantial increase in mass efficiency, suggesting a correlation between system miniaturization and performance.

While the tensional architecture investigated in this study outperforms traditional linear actuators by an order of magnitude, its measured power density of $125\,\mathrm{W\,kg^{-1}}$ remains well below the theoretical limit for NiTi-based SMAs reported by [12], indicating that the full performance potential of the material has not yet been realized.

Table I provides a summary of the key performance metrics for each actuator type.

These results demonstrate that SMA-based solutions—especially when configured in efficient architectures such as the tensional configuration—offer lightweight, power-efficient alternatives. The presented framework enables informed actuator selection based on application-specific constraints such as mass, volume, or power availability, and paves the way for more adaptable and sustainable actuation strategies in space systems.

REFERENCES

[1] M. Sakovsky, J. Trutna, T. Sinn, A. Pedivellano, M. Geiss, and N. Eker, "Shape Changing Structures for Adaptive Space Structure Applications," in *73rd International Astronautical Congress (IAC)*, Sep. 2022.

[2] O. Testoni, T. Lumpe, J.-L. Huang, M. Wagner, S. Bodkhe, Z. Zhakypov, R. Spolenak, J. Paik, P. Ermanni, L. Muñoz, and K. Shea, "A 4D printed active compliant hinge for potential space applications using shape memory alloys and polymers," *Smart Materials and Structures*, vol. 30, no. 8, p. 085004, Jun. 2021.

[3] J. Schmidt and M. Sakovsky, "Model-based design of an antagonistic shape memory alloy actuator for bistable morphing structures," in *Proceedings of [Insert Conference Name]*, Garching, Germany and Stanford, CA, USA, 2024, to appear. Funding agency acknowledgment and full publication details to be added.

[4] EBAD, "TiNi™ Frangibolt® Actuator to Support and Release Loads - EBAD," https://ebad.com/products/tini-frangibolt/, 2025.

[5] Dcubed, "Pin Pullers - Dcubed," https://dcubed.space/products/pin-pullers/, 2025.

[6] K. Tanaka, S. Kobayashi, and Y. Sato, "Thermomechanics of transformation pseudoelasticity and shape memory effect in alloys," *International Journal of Plasticity*, vol. 2, no. 1, pp. 59–72, Jan. 1986.

[7] L. C. Brinson, "One-Dimensional Constitutive Behavior of Shape Memory Alloys: Thermomechanical Derivation with Non-Constant Material Functions and Redefined Martensite Internal Variable," *Journal of Intelligent Material Systems and Structures*, vol. 4, pp. 229–242, 1993.

[8] X. Gao, R. Qiao, and L. Catherine Brinson, "Phase diagram kinetics for shape memory alloys: A robust finite element implementation," *Smart Materials and Structures*, vol. 16, no. 6, p. 2102, Oct. 2007.

[9] S.-M. An, J. Ryu, M. Cho, and K.-J. Cho, "Engineering design framework for a shape memory alloy coil spring actuator using a static two-state model," *Smart Materials and Structures*, vol. 21, no. 5, p. 055009, Apr. 2012.

[10] J. V. Humbeeck, "Cycling effects, fatigue and degradation of shape memory alloys," *Le Journal de Physique IV*, vol. 1, no. C4, pp. 184–197, Nov. 1991.

[11] Y. Zhang, W. Li, Z. Moumni, J. Zhu, W. Zhang, and S.-Y. Zhong, "Degradation of the recoverable strain during stress controlled full transformation cycling in NiTi shape memory alloys," *Scripta Materialia*, vol. 162, pp. 68–71, Mar. 2019.

[12] C. H. Park, S. Y. Ham, and Y. S. Son, "Relationship between input power and power density of SMA spring," in *Active and Passive Smart Structures and Integrated Systems 2016*, G. Park, Ed. SPIE, Apr. 2016.

[13] "LA30 Series — inspire-robots.store," https://inspire-robots.store/products/la30-series?srsltid=AfmBOoqcjgY1Zr-xCIzSuEZo6xlbagW6JpLQBntMuFVSjypeo1FK9NkY&variant=42720195870964, 2024, [Accessed 06-12-2024].